Journal of Magnetic Resonance 270 (2016) 187–197

Contents lists available at ScienceDirect

Journal of Magnetic Resonance

journal homepage: www.elsevier.com/locate/jmr

Fast imaging of laboratory core floods using 3D compressed sensing RARE MRI

N.P. Ramskill [a,*], I. Bush [a], A.J. Sederman [a], M.D. Mantle [a], M. Benning [b], B.C. Anger [c], M. Appel [c], L.F. Gladden [a]

[a] Department of Chemical Engineering and Biotechnology, University of Cambridge, Pembroke Street, Cambridge CB2 3RA, UK
[b] Department of Applied Mathematics and Theoretical Physics, University of Cambridge, Wilberforce Road, Cambridge CB3 0WA, UK
[c] Shell Technology Centre, 3333 Highway 6 S, Houston, TX, USA

ARTICLE INFO

Article history:
Received 16 March 2016
Revised 26 July 2016
Accepted 27 July 2016
Available online 29 July 2016

Keywords:
Magnetic resonance imaging
Compressed sensing
Porous media
Petrophysics
Core analysis

ABSTRACT

Three-dimensional (3D) imaging of the fluid distributions within the rock is essential to enable the unambiguous interpretation of core flooding data. Magnetic resonance imaging (MRI) has been widely used to image fluid saturation in rock cores; however, conventional acquisition strategies are typically too slow to capture the dynamic nature of the displacement processes that are of interest. Using Compressed Sensing (CS), it is possible to reconstruct a near-perfect image from significantly fewer measurements than was previously thought necessary, and this can result in a significant reduction in the image acquisition times. In the present study, a method using the Rapid Acquisition with Relaxation Enhancement (RARE) pulse sequence with CS to provide 3D images of the fluid saturation in rock core samples during laboratory core floods is demonstrated. An objective method using image quality metrics for the determination of the most suitable regularisation functional to be used in the CS reconstructions is reported. It is shown that for the present application, Total Variation outperforms the Haar and Daubechies3 wavelet families in terms of the agreement of their respective CS reconstructions with a fully-sampled reference image. Using the CS-RARE approach, 3D images of the fluid saturation in the rock core have been acquired in 16 min. The CS-RARE technique has been applied to image the residual water saturation in the rock during a water-water displacement core flood. With a flow rate corresponding to an interstitial velocity of $v_i = 1.89 \pm 0.03$ ft day^{-1}, 0.1 pore volumes were injected over the course of each image acquisition, a four-fold reduction when compared to a fully-sampled RARE acquisition. Finally, the 3D CS-RARE technique has been used to image the drainage of dodecane into the water-saturated rock in which the dynamics of the coalescence of discrete clusters of the non-wetting phase are clearly observed. The enhancement in the temporal resolution that has been achieved using the CS-RARE approach enables dynamic transport processes pertinent to laboratory core floods to be investigated in 3D on a timescale and with a spatial resolution that, until now, has not been possible.

1. Introduction

Laboratory-scale displacements in rock core-plug samples (core floods) are widely used to develop understanding of oil recovery mechanisms [1–5], for validating interpretations of field-pilot well logging data [2] and for oilfield evaluation [3,4]. Traditionally, dynamic monitoring of core-plug internal fluid distributions has not been possible. This limitation necessitates that the system is treated as a 'black-box', whereby only the volumes and compositions of recovered fluids can be determined [5]. In reality, accurate recoveries cannot be determined from such volumetric averages, due to capillary end effects, oil bank formations, and both structural and surface wettability heterogeneities [2,4,6–9]. To this end, acquiring spatially-resolved information on the fluid distributions occurring throughout the time-course of core-floods is of considerable interest.

Currently, magnetic resonance imaging (MRI) [1,2,4–6,10–23] and X-ray computed tomography (CT) [24–29] are the most widely used techniques for imaging *in situ* core flood fluid distributions; both of which can non-destructively image multiphase fluid systems in porous media. As is well known the origin of image contrast associated with the two methodologies is quite different [30]. Whilst X-ray CT produces images at higher spatial resolution than MRI, albeit typically on smaller samples, the range of non-invasive contrast mechanisms associated with MRI methods, combined with its existing applications in special core analysis

* Corresponding author.
E-mail address: npr24@cam.ac.uk (N.P. Ramskill).

http://dx.doi.org/10.1016/j.jmr.2016.07.017
1090-7807/

(porosity, permeability [31–33], surface interaction and wettability [34] measurements) make using magnetic resonance for imaging laboratory core floods a natural choice [35].

In systems that exhibit an heterogeneous fluid distribution within the rock during the core flood, for instance due to the capillary end effect [9], formation of Saffman-Taylor instabilities [12,36] or so-called 'worm holes' in reactive flow [37], 3D images are required to fully characterise core-flood behaviour. In conventional MRI acquisitions, **k**-space data are uniformly sampled at the Nyquist rate at increments of $\Delta\mathbf{k}$, which is determined by the desired field-of-view (FOV) and image resolution [38,39]. Consequently, when multi-dimensional and high spatial resolution images are sought, this can result in long acquisition times. For example, when using the spin-warp pulse sequence [40] for a matrix size of $256 \times 128 \times 128$ (read $\times$ phase $\times$ phase) with a recycle time of 2 s and 4 scans for signal averaging, the acquisition time will be approximately 36 h. At an interstitial velocity of 1 ft day^{-1}, which is representative of that found in the reservoir, in a 1.5″ diameter by 3″ length cylindrical plug with a porosity of 20%, approximately seven pore volumes (P.V.) of the displacing fluid will have been injected over the course of the 36 h acquisition. From this it is evident that the acquisition times for conventional 3D MRI sequences are such that the dynamic nature of core flood displacements cannot be effectively monitored.

Image acquisition times can be reduced using fast imaging sequences such as Rapid Acquisition with Relaxation Enhancement (RARE) [41] and Echo Planar Imaging (EPI) [42]. The principle behind both RARE and EPI is that multiple lines of **k**-space are acquired from an individual excitation. The practical limit on the number of lines of data that can be acquired from each excitation, and correspondingly the reduction in acquisition time, is determined by the relaxation times of the sample under investigation. The transverse relaxation times for the fluid-saturated rock core samples, which are the subject of the present study, are expected to be in the range of tens to hundreds of milliseconds. Considering a RARE acquisition of a water-saturated rock core characterised by T_2 = 150 ms, with an echo time T_E = 4 ms, it is reasonable to suggest that 32 lines of **k**-space can be acquired from each excitation. Therefore, for a matrix size of $256 \times 128 \times 128$ (read $\times$ phase $\times$ phase) with a recycle time of 2 s and 4 scans for signal averaging, the acquisition time is approximately 68 min. For the same conditions of the hypothetical core-flood discussed previously, approximately 0.2 P.V. of the displacing fluid will have been injected during the course of the acquisition. Whilst this is a significant improvement relative to the spin-warp acquisition, it is desirable to reduce the amount of blurring over the image acquisition still further to ensure that 'snap-shots' of the fluid distribution can be acquired at specific time points during the core flood.

It has been demonstrated that by using compressed sensing (CS), a signal with a sparse representation, such as an image, can be recovered from a number of measurements sampled below the Nyquist rate [43,44]. It therefore follows that by combining CS with ultra-fast MRI acquisitions, further reductions in acquisition time can be achieved, thus enabling dynamic processes, such as the laboratory core flood, to be studied. A second advantage of the enhancement in temporal resolution using CS is that a higher signal-to-noise ratio (SNR) can be achieved through more signal averaging per unit acquisition time. Again, this is desirable to the petrophysics community as low-field magnets, with inherently low sensitivity, are commonly used in a core analysis laboratory.

In application to porous materials, CS has previously been combined with pure phase-encoding techniques. Due to their robustness in the presence of paramagnetic impurities and magnetic susceptibility gradients, the pure phase encode methods have proven to be suitable for providing quantitative measurements of the fluid content in particularly challenging systems, such as rock cores. Single point imaging (SPI) with CS has been employed to quantitatively 3D-image dynamic moisture absorption processes within cereal-based wafer material [45]. Under-sampling the acquisition (at 33% of **k**-space) reduced the acquisition time from 39 to 13 min. More recently, spin echo SPI (SESPI) was used to image a water-saturated Berea sandstone core-plug: under-sampling in both phase-encoding directions, in which 20% of a 64×32 **k**-space matrix was acquired, resulted in an acquisition time of 2 h, which represented a 5-fold enhancement in the temporal resolution relative to a fully-sampled acquisition [46].

CS has also been compared with restricted **k**-space 'keyhole' imaging to provide spatially-resolved, 2D T_2 distributions [47]. While it was determined that the keyhole approach was more robust than CS in obtaining T_2 distributions from the image, both methods were found to be able to produce spin density maps in close-agreement with the fully-sampled reference image. However, there is an inherent limitation of the keyhole method when it cannot be assumed that the high spatial frequency regions of **k**-space, that are not sampled, do not change significantly over the time-course of experiments. The idea of restricted **k**-space sampling, as a means of decreasing acquisition times, has since been extended to obtain 2D Hybrid-SESPI, as well as 2D and 3D SPRITE images [48]. Xiao and Balcom [49] have presented a method using SESPI to acquire 1D water-saturation profiles during the dynamic flooding of a sandstone rock core. It has been shown that correlations in the spatial and temporal dimensions can be exploited to enable under-sampling of **k**-*t*-space, thus resulting in significant reductions in the acquisition time.

However, even with **k**-space under-sampling, the pure phase encoding techniques are too slow for studying dynamic displacement processes with 3D MRI. Depending on the system under investigation and the information sought, the choice of MRI pulse sequence is a trade-off between how quantitative the resulting image is and the achievable temporal resolution. In the application to imaging of rock cores, the most commonly used fast imaging techniques are π-EPI (PEPI) [50] and RARE [41]. The latter has certain advantages over the former, in that it is both T_1 and T_2-weighted as opposed to solely T_2-weighted, which, in theory, means that the signal lifetime is longer and more echoes may be acquired from a single excitation for a given echo time [35]. Additionally, due to non-ideal radio frequency (r.f.) pulses and imperfect gradients, PEPI is a notoriously difficult pulse sequence to implement. However, it has been shown by Xiao and Balcom [51] that by using composite broadband refocusing r.f. pulses and gradient pre-equalization, 3D PEPI can be successfully implemented to image water saturation in rock core plugs. This method has recently been applied to measure the oil distribution within a rock during a dynamic core flood [52]. As will be discussed in detail in Section 3, the RARE pulse sequence is particularly well-suited to CS acquisitions. This is due to the fact that the magnetisation is returned to the same position in **k**-space following the acquisition of each echo thus allowing much greater freedom in the design of the **k**-space sampling patterns. Considering the relative merits of these two ultra-fast MRI sequences, the RARE pulse sequence will be used as the basis for the CS acquisitions in the present study.

In this work, a 3D RARE with CS technique is demonstrated for imaging the fluid saturation during a laboratory core flood. The optimal **k**-space under-sampling strategy and image reconstruction protocols are described. The 3D CS-RARE technique is then applied to monitoring the forced displacement of water from a Bentheimer sandstone and subsequently the injection of dodecane into the water-saturated rock.

2. Compressed sensing theory

The concepts underpinning CS applied to MRI, and the mathematical formalism used is described by Lustig et al. [43]. The approach used in the present work and described below follows this approach. The particular regularisation methods and image quality metrics used here are introduced in our earlier work [53]. The successful implementation of CS in MRI is based on the following requirements: (1) the aliasing artefacts in the linear reconstruction must be incoherent and noise-like; (2) the desired image exhibits transform sparsity; and (3) the image is reconstructed using a non-linear algorithm that enforces sparsity and consistency with the acquired **k**-space data.

Let us consider the case where the image to be reconstructed is given by **x** which is related to the acquired **k**-space measurements via:

$$S\mathbf{F}\mathbf{x} + v = \mathbf{y}, \tag{1}$$

where S is the sub-sampling pattern, **F** is the Fourier transform that maps the image into **k**-space, v is the normally-distributed noise (standard deviation σ and zero mean) and **y** is the vector that contains the acquired **k**-space measurements. Due to under-sampling and the presence of noise, Eq. (1) is an ill-posed problem and therefore linear image reconstruction methods, such as the inverse Fourier transform, which is typically employed for the image reconstruction of a fully-sampled **k**-space data set, will result in an image containing aliasing artefacts due to the violation of the Nyquist criterion. Therefore an approximate solution to **x** is sought by using a variational regularization approach balancing the model (Eq. (1)) and prior assumptions of **x** in terms of a regularisation functional J given by:

$$\begin{aligned} &\mathbf{x}_\sigma \in \arg\min_\sigma J(\mathbf{x}) \\ &\text{subject to } \|S\mathbf{F}\mathbf{x} - \mathbf{y}\|_2 \leqslant \sigma. \end{aligned} \tag{2}$$

The role of the inequality constraint enforces consistency with the acquired **k**-space data and the regularization term J incorporates prior information on the reconstruction of $\mathbf{x}_\sigma$, which is required to counteract the ill-posedness of the problem.

In the case of the CS reconstruction, the prior information is that the image can be sparsely represented either implicitly or in an appropriate transform domain. Typically, the choice of the regularisation functional (J) that is used to map the image into the transform domain depends on the nature of the image to be reconstructed. For instance, Total Variation (TV) may be more suited to an image with sharp-edges whereas the Daubechies wavelet transform lends itself well to images in which the pixel intensities change more gently [53]. In the present study, TV and two families of wavelet transforms have been considered as the regularisation functionals, $J(\mathbf{x})$, as will now be discussed:

Total Variation penalises the 1-norm of the 2-norm of the finite different approximation of the gradient (∇) of the image as given by:

$$J(\mathbf{x}) = TV\mathbf{x} = \|\nabla\mathbf{x}\|_{2,1}. \tag{3}$$

In the present study, Neumann boundary conditions were set for the CS reconstructions.

Wavelet transforms penalise the 1-norm of the wavelet-transform (W) of the image as given by:

$$J(\mathbf{x}) = WAV\mathbf{x} = \|W\mathbf{x}\|_1. \tag{4}$$

In the present study, the six-level Haar and Daubechies3 wavelet transform of the image have been considered as examples of W.

Generally, the Tikhonov-Regularization scheme for the approximation of **x** is written as:

$$\mathbf{x}_\alpha \in \arg\min \left\{ \frac{1}{2}\|\mathbf{y} - S\mathbf{F}\mathbf{x}\|_2^2 + \alpha J(\mathbf{x}) \right\} \tag{5}$$

where the regularisation parameter α (always positive) weights the influence of the fidelity and regularisation terms in Eq. (5). In the present study, a modification of Eq. (5) to include Bregman iterations [53] has been implemented as described by Eq. (6):

$$\mathbf{x}_\alpha^k \in \arg\min \left\{ \frac{1}{2}\|\mathbf{y}^k - S\mathbf{F}\mathbf{x}\|_2^2 + \alpha J(\mathbf{x}) \right\}, \tag{6a}$$

$$\mathbf{y}^k = \mathbf{y}^{k-1} + \mathbf{y} - S\mathbf{F}\mathbf{x}_\alpha^k. \tag{6b}$$

Using the Bregman approach, a series of k problems (Eq. (6a)) are solved with the residual added to the **k**-space data, **y**, after each iteration (Eq. (6b)). The computational realisation of this approach that has been employed in the present study is described in detail elsewhere [53]. The 3D CS reconstructions were performed in Matlab 2014a (Mathworks, USA) and image post-processing was performed in Avizo Fire 8.1 (FEI Visualisation Sciences Group, USA).

3. Implementation of the 3D CS-RARE method

In the following section, the three key elements for the implementation of the 3D CS-RARE method are presented. Firstly, the pulse sequence that has been used as the basis for MRI acquisitions will be described. Secondly, the rationale for the choice of **k**-space under-sampling scheme and the approach for how these data are acquired experimentally are shown. Finally, an objective method for the determination of the choice of regularisation functional and permissible level of under-sampling to be used in the CS-RARE acquisitions is demonstrated.

3.1. 3D CS-RARE acquisitions

The RARE pulse sequence (Fig. 1) has been used as the basis for the MRI. To enable freedom in the sampling patterns to be used for the CS acquisitions, the first and second phase-encoding gradients, G_{P1} and G_{P2} respectively, are incremented N_{RF} times simultaneously within the train of echoes following each r.f. excitation, where N_{RF} is the RARE-factor.

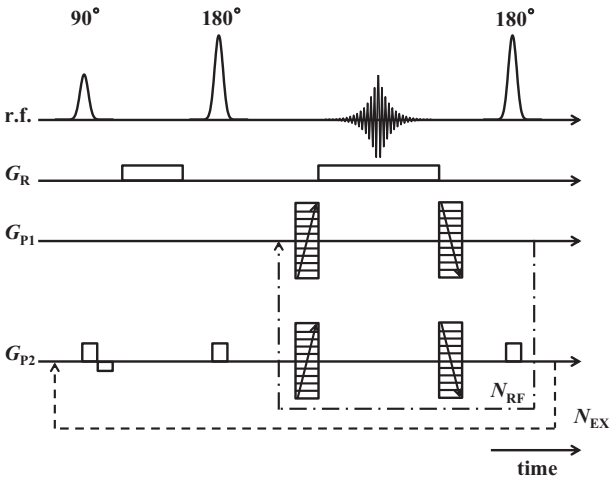

Fig. 1. Schematic of the Rapid Acquisition with Relaxation Enhancement (RARE) pulse sequence. **k**-space is frequency encoded in the read direction (k_R) and phase encoded in k_{P1} and k_{P2} upon the application of the read gradient (G_R) and phase gradients (G_{P1} and G_{P2}) respectively. The number of 180° degree pulses applied for each acquisition is determined by the RARE factor (N_{RF}) and the total number of r.f. excitations (N_{EX}) required to sample **k**-space is given by the total number of points in the two phase encoding directions, $N_{P1,2}$ divided by N_{RF}.

Referring to Fig. 1, **k**-space is frequency encoded in the read direction (k_R) and phase encoded in the phase directions k_{P1} and k_{P2} upon the application of the read gradient (G_R) and phase gradients (G_{P1} and G_{P2}) respectively. For a fully-sampled 3D RARE acquisition, the total experiment time is proportional to $(N_{P1} \times N_{P2})/N_{RF}$, where N_{P1} and N_{P2} are the number of points in the first and second phase encoding directions, respectively. From this expression, it is evident that the acquisition time can be reduced by increasing N_{RF} and reducing N_{P1} and N_{P2}. However, the maximum N_{RF} that can be used is limited by the relaxation times of the system, and N_{P1} and N_{P2} are fixed by the image resolution.

3.2. *k*-space under-sampling protocol

As has been discussed previously, using CS it is possible to reconstruct an image from under-sampled **k**-space data. In the case of 3D-RARE acquisitions, this implies that fewer measurements in the two phase encoding dimensions (k_{P1} and k_{P2}) can be made than would be the case for the fully-sampled acquisitions, thus leading to reductions in the total experiment time. As there is no significant time penalty associated with frequency encoding, **k**-space is fully-sampled in the read-out dimension (k_R).

To ensure that the *true* signal in the image can be recovered effectively in the CS reconstruction, it is important that the artefacts arising from sub-Nyquist rate sampling add incoherently, and appear noise-like, in the image domain [43,44,54]. By sampling **k**-space randomly, high levels of artefact incoherence in the linear transform can be achieved. However, considering the shape of the **k**-space signal, it has been shown that preferentially sampling towards the centre of **k**-space may be optimal. Therefore, in the present study, k_{P1} and k_{P2} are sampled according to a pseudo-random, variable-density sampling pattern weighted towards the centre of **k**-space. The methodology used for the generation of the **k**-space sampling pattern is based on the Monte-Carlo incoherent sampling design approach developed by Lustig et al. [43].

Two possible under-sampling approaches have been considered: Scheme 1 – two-dimensional variable-density in k_{P1} and k_{P2}; Scheme 2 – k_{P1} and k_{P2} are under-sampled, independently of one another, using a variable density approach. Representative sampling patterns for Scheme 1 and Scheme 2, for 50% sampling of **k**-space, are shown in Fig. 2a and b, respectively.

In order to assess which of the sampling methods is optimal, the Shepp-Logan phantom has been considered. Artificial fully-sampled **k**-space data (Fig. 3a) has been generated from the Fourier transform of the Shepp Logan phantom (Fig. 3d). From this, under-sampled **k**-space data have been obtained *via* the element-by-element multiplication of the fully-sampled **k**-space (Fig. 3a) with the two sampling patterns (Fig. 2). The **k**-space data derived from Scheme 1 (Fig. 2a) and Scheme 2 (Fig. 2b) are shown in Fig. 3b and c, respectively. The Fourier transform of the zero-filled **k**-space data are shown in Fig. 3e and f, respectively. It can be seen that in the linear reconstruction from the under-sampled **k**-space data from Scheme 1 (Fig. 3e), the artefacts appear to be noise-like whereas they appear to be somewhat more coherent in the linear reconstruction from the under-sampled **k**-space data from Scheme 2 (Fig. 3f). From this, it is evident that Scheme 1 is the more suitable method of under-sampling **k**-space in terms of maximising the incoherence of the aliasing artefacts in the reconstruction and will therefore be employed in the CS acquisitions.

To demonstrate how the 3D CS-RARE acquisition has been employed experimentally, Fig. 4 shows a sampling pattern with 25% of a 128×128 matrix (i.e. 4096 points) in the k_{P1} and k_{P2} dimensions, respectively. Each white pixel represents a point in k_{P1} and k_{P2} at which a line of **k**-space in the read direction, k_R (into the page) is fully-sampled.

In an attempt to ensure that relaxation weighting of the signal is consistent across **k**-space, a key consideration is the order in which the points are acquired. In the standard implementation of 3D RARE, for each excitation, N_{RF} lines of k_R are acquired at different positions in k_{P1} for a single value of k_{P2} and this is repeated for all values of k_{P2} for subsequent excitations. However, given the variable-density nature of the sampling pattern (Fig. 4), this is not feasible as the number of points sampled in k_{P1} is not constant for all values of k_{P2}. To this end, an approach whereby the points in $k_{P1,2}$ are sampled in an order corresponding to their proximity from the centre of **k**-space has been implemented. Fig. 5a shows a representative trajectory for k_{P1} and k_{P2} as a function of the number of 180° pulses in the RARE loop for one excitation where $N_{RF} = 64$. Therefore, for the case where $N_{RF} = 64$, 64 r.f. excitations and different sets of gradient values are required to sample all 4096 lines of k_R in $k_{P1,2}$ as shown in Fig. 5b.

From Fig. 5a it is evident that the centre of **k**-space (in the two phase-encoding directions) is approached around the 32nd 180° pulse for each excitation. It should be noted that using this method, the point at which the centre of **k**-space is approached within the train of 180° pulses can be optimised depending on the nature of

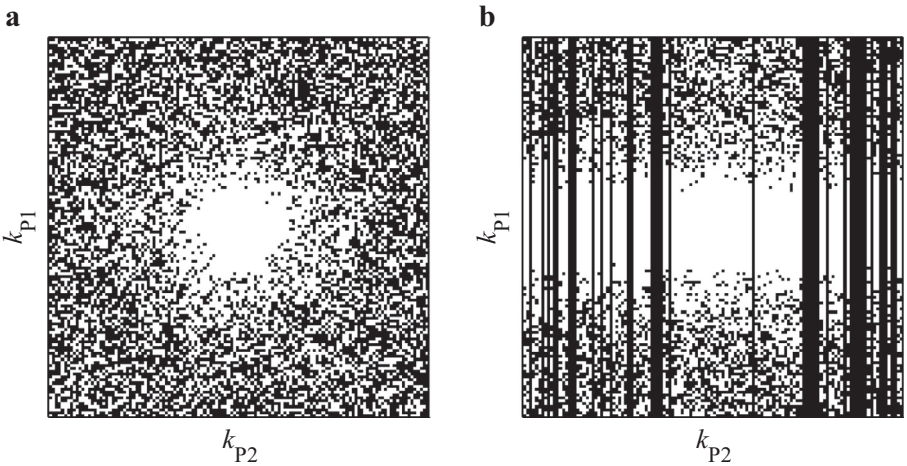

Fig. 2. Representative **k**-space sampling patterns for (a) Scheme 1: two-dimensional variable density, pseudo random and (b) Scheme 2: series of one-dimensional variable density, pseudo random methods, for 50% under-sampling. The white pixels represent positions in k_{P1} and k_{P2} at which a line of k_R (into the page) is fully sampled, whilst the black pixels are not sampled.

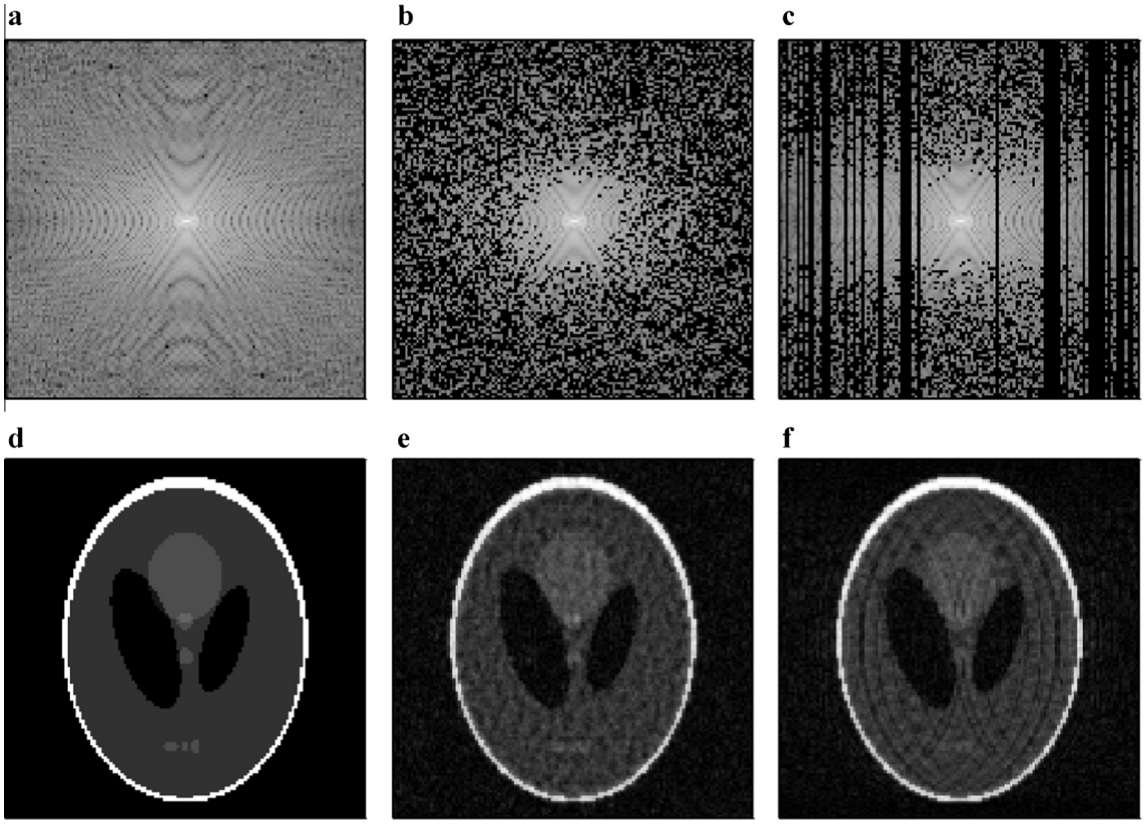

Fig. 3. (a) Artificial **k**-space generated from the (b) Shepp-Logan phantom. Under-sampled **k**-space and the associated zero-filled Fourier transform for under-sampling method Scheme 1 (b and e) and Scheme 2 (c and f). Referring to the under-sampled **k**-space rasters (b and c), the black pixels indicate positions in k_{P1} and k_{P2} that are not sampled.

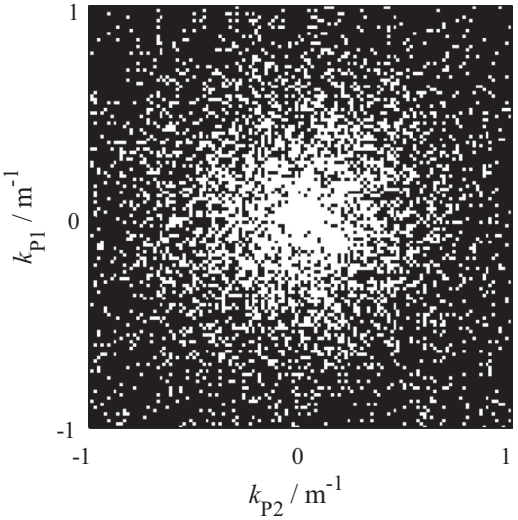

Fig. 4. Variable-density **k**-space sampling pattern with under-sampling in the two phase encoding directions for a sampling fraction of 25% of a 128 × 128 matrix. The white pixels represent positions in k_{P1} and k_{P2} at which a line of k_R (into the page) is fully sampled.

the system under investigation. For instance, approaching the centre of **k**-space earlier would improve the SNR at the expense of the high-resolution features in the image. From Fig. 5b, it can be seen the same regions of **k**-space are acquired at approximately the same point in each train of echoes, thus ensuring that relaxation weighting is distributed evenly across **k**-space.

3.3. Image quality metrics

To determine the most suitable regularisation functional to use in the CS reconstructions and the degree to which **k**-space can be under-sampled in the CS-RARE acquisitions, an objective assessment of the quality of the images obtained from the CS reconstructions ($\mathbf{x}_{CS}$) with respect to a fully sampled reference image ($\mathbf{x}_{FS}$) has been conducted. For this, commonly used metrics of image quality, ℓ_2-error, peak signal-to-noise ratio (PSNR) and the structural similarity index (SSIM), as will now be described, have been used:

3.3.1. ℓ_2-error

The ℓ_2-error of the difference map between the fully-sampled and CS reconstructions is used as a simple, quantitative measure of the quality of the CS reconstruction relative to the fully-sampled image as given by:

$$\ell_2 = \frac{\|\mathbf{x}_{CS} - \mathbf{x}_{FS}\|_2}{\|\mathbf{x}_{FS}\|_2}. \tag{7}$$

The ℓ_2 norm of the matrix is defined as $\|x\|_2 = \sqrt{\sum_i |x_i|^2}$ where x_i is the signal intensity at the ith voxel. A lower ℓ_2-error indicates a better quality reconstruction.

3.3.2. Peak signal-to-noise ratio

The peak signal-to-noise ratio (PSNR) is a frequently used metric for assessing the quality of an image reconstruction and is given by:

$$\mathrm{PSNR}(\mathbf{x}_{CS}, \mathbf{x}_{FS}) = 10\log_{10}\left(\frac{L}{\|\mathbf{x}_{CS} - \mathbf{x}_{FS}\|_2^2 / N_{vox}}\right), \tag{8}$$

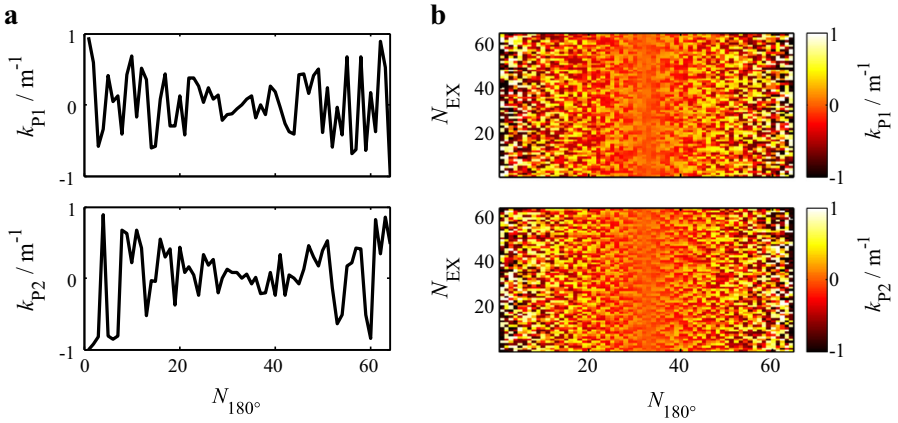

Fig. 5. (a) Representative trajectories for k_{P1} and k_{P2} as a function of the number of 180° pulses in the RARE loop for a single excitation. It can be seen that the centre of **k**-space (in the two phase-encoding directions) is approached around the 32nd 180° pulse. (b) Stacked plot of the 64 different gradient trajectories required for the 3D CS-RARE acquisition.

where $L = \max |\mathbf{x}_{FS}|$ and $N_{vox} = N_{P1}N_{P2}N_{P3}$. A higher value of PSNR indicates a better quality reconstruction.

3.3.3. Structural similarity index

The structural similarity (SSIM) index has been shown to be a particularly robust metric in quantifying structural differences between a distorted and reference image [55]. Preservation of the structural features in the CS-reconstructed images is of the utmost importance and hence the SSIM index is a particularly relevant metric in application to imaging rock cores. The local SSIM (LSSIM) index is given by:

$$\mathrm{LSSIM}(\mathbf{x}_{CS}, \mathbf{x}_{FS}) = \frac{(2\mu_{\mathbf{x}_{FS}}\mu_{\mathbf{x}_{CS}} + C_1)(2\sigma_{\mathbf{x}_{FS}}\sigma_{\mathbf{x}_{CS}} + C_2)}{(\mu^2_{\mathbf{x}_{FS}} + \mu^2_{\mathbf{x}_{CS}} + C_1)(\sigma^2_{\mathbf{x}_{FS}} + \sigma^2_{\mathbf{x}_{CS}} + C_2)} \quad (9)$$

where μ and σ are the mean and standard deviation, respectively, of the image intensity in a local Gaussian-weighted window. The global SSIM is obtained by averaging the LSSIM estimates across the entire image. The constants ($C_1 = 0.01L$ and $C_2 = 0.03L$) are included to avoid instabilities. A perfect reconstruction would yield an SSIM = 1.

4. Experimental

4.1. Materials

A Bentheimer sandstone plug, 37.5 ± 0.1 mm in diameter and 70.5 ± 0.1 mm in length, has been used as a representative sample of a hydrocarbon-bearing reservoir rock. The pore volume (P.V.) of the rock was determined by gravimetric analysis to be 17.6 ± 0.1 ml, thus corresponding to a porosity of $\varphi = 23 \pm 2\%$. For the MRI measurements, the sample was held in an Aflas sleeve within a PEEK rock core holder (ErgoTech, Conwy, UK). A constant confining pressure was applied to the outside of the Aflas sleeve by per-fluorinated oil (Fluorinert FC-43) using a Gilson 307 (Gilson Inc., USA) HPLC pump maintained at 250 ± 25 psig by a back pressure regulator (Idex Health and Science, USA).

4.2. Magnetic resonance imaging

The MRI experiments were carried out on a 2 T (85 MHz for ^{1}H) horizontal-bore magnet controlled by a Bruker AV spectrometer. A 60 mm r.f. coil tuned to a frequency of 85.2 MHz was used for excitation and signal detection. Spatial resolution was achieved with magnetic field gradients with a maximum strength of 10.7 G cm^{-1}. The RARE pulse sequence (Fig. 1) was used to acquire both fully- and under-sampled 3D images. Gaussian-shaped 90° excitation and 180° refocusing r.f. pulses of duration 512 μs and power levels of 27 dB and 21 dB, respectively were used. Typical echo times for the RARE acquisitions were approximately $T_E = 4$ ms. The logarithmic mean of the longitudinal and transverse relaxation time distributions of the water-saturated Bentheimer rock core were measured to be $T_{1LM} = 150$ ms and $T_{2LM} = 120$ ms, respectively.

4.2.1. Fully-sampled 3D RARE image

A fully-sampled 3D image of a water-saturated Bentheimer sandstone rock core was acquired as a reference image to be used in the analysis presented in Section 5.1 and 5.2 to determine the most suitable regularisation functional to use in the CS reconstructions and to determine the degree to which **k**-space can be undersampled in the CS-RARE acquisitions, respectively. The field-of-view (FOV) was 80 mm × 50 mm × 50 mm in the *z*, *x* and *y* directions respectively. For the data matrix size of 256 × 128 × 128 pixels used in the read (*z*) direction and first (*x*) and second (*y*) phase encoding directions, the image resolution is therefore 0.31 mm pixel^{-1} × 0.39 mm pixel^{-1} × 0.39 mm pixel^{-1}. With a RARE factor of $N_{RF} = 32$ and eight scans for signal averaging, the acquisition time was approximately 2 h 9 min.

4.2.2. 3D CS-RARE imaging during laboratory core flood displacements

For the core flood experiments, two separate experiments were performed on the same rock core. First, the rock was initially saturated with deionised water, which was subsequently displaced by a gadolinium chloride ($GdCl_3$) doped-water solution during the core flood. A $GdCl_3.6H_2O$ concentration of ~8 mM was used, such that the resulting T_2 of the solution was ~10 ms, and was therefore sufficiently short that it could not be detected in the images. The injectant was pumped through the rock at a flow rate of 0.1 ml min^{-1} using a Quizix QX1500 (Chandler Engineering, USA) dual-syringe pump. The corresponding interstitial pore velocity is, $v_i = 1.89 \pm 0.03$ ft day^{-1}. During the core flood, a series of 3D CS-RARE images were acquired to image the residual water content (i.e. the undoped water remaining in the rock) until all of the undoped water had been displaced by the Gd^{3+}-doped solution. In the second experiment, the core from the experiment (now saturated with the Gd^{3+}-doped solution) was taken, and dodecane was injected at 0.1 ml min^{-1} using a Harvard 22 syringe pump (Harvard Apparatus, USA) to mimic a primary drainage process. Again, a series of 3D CS-RARE images were acquired during this process.

All of the images were acquired with a FOV of 80 mm × 50 mm × 50 mm in the *z*, *x* and *y* directions respectively. For a data matrix size of 256 × 128 × 128 pixels in the read (*z*) direction and first (*x*) and second (*y*) phase encoding directions, this gave an image resolution of 0.31 mm pixel^{-1} × 0.39 mm pixel^{-1} × 0.39 mm pixel^{-1}. With a 25% sampling of **k**-space, a RARE factor of $N_{RF} = 64$ and eight scans for signal averaging, the acquisition time was ~16 min.

5. Results and discussion

The results are presented in three sections. Firstly, a justification for the most suitable regularisation functional to be used for the CS image reconstructions is presented. Secondly, a series of CS reconstructions on artificially under-sampled **k**-space data have been conducted to determine the level of under-sampling to be used for the CS-RARE acquisitions. Finally, the 3D CS-RARE method has been used to image the residual water saturation during the forced displacement by a doped-water solution and subsequently to image the drainage of dodecane into the water-saturated rock core.

5.1. Investigation of regularisation functionals

In this section, the images obtained from CS reconstructions ($\mathbf{x}_{CS}$) using different regularisation functionals described in Section 2 have been compared with a fully-sampled ($\mathbf{x}_{FS}$) reference image using the image quality metrics described in Section 3.3. Artificially under-sampled **k**-space data were generated by multiplying the 3D **k**-space data, acquired for the fully-sampled image of the water-saturated Bentheimer, by a variable-density sampling pattern (e.g. Fig. 4) with a sampling fraction of 25%. For the CS reconstructions of the under-sampled **k**-space data, 20 Bregman iterations (Eqs. (6a) and (6b)) were performed; the starting value of the regularisation parameter was $\alpha = 0.1$ in all cases. Subsequently, the image quality metrics, ℓ_2-error (Eq. (7)), PSNR (Eq. (8)) and SSIM (Eq. (9)), were determined for the 3D images obtained following each of the Bregman iterations as shown in Fig. 6a–c, respectively.

Two-dimensional *xz* slice images from the central plane of the 3D images obtained from the fully-sampled reconstruction and zero-filled Fourier transform are shown in Figs. 7a and b, respectively. As discussed in Section 3.3, the best CS reconstructions are deemed to be the images that yield the lowest ℓ_2-error and the highest PSNR and SSIM. Therefore, referring to Fig. 6, the best images for the CS reconstructions using TV, Haar wavelet transform and Daubechies-3 wavelet transform as the regularization functional correspond to Bregman iteration numbers 20, 3 and 3 and are shown in Fig. 7c, d and e, respectively.

Considering the fully-sampled image of the water-saturated rock (Fig. 7a), the choice of the most suitable regularisation functional to use in the CS reconstruction is not immediately apparent as there is no obvious sparse representation of the image in any of the transform domains that have been considered. Nevertheless, it is clear that all three CS reconstructions (Fig. 7c–e) recover an image that is much more visually similar to the fully-sampled case than the zero-filled Fourier transform (Fig. 7b) and therefore the use of CS is justified. From the image quality analysis presented in Fig. 6, of the different regularisation functionals considered, TV yields the best image quality with respect to the fully-sampled image. For a 25% **k**-space sampling fraction, an image with an ℓ_2-error = 0.18, PSNR = 32.5 and an SSIM = 0.86 is recovered. For the same level of under-sampling, the best-performing wavelet transform is the Haar function which yielded an image with an ℓ_2-error = 0.26, PSNR = 29.6 and an SSIM = 0.74. Based on these results, TV will be used for all subsequent CS reconstructions in the present study.

5.2. Level of under-sampling for CS-RARE acquisitions

In order to determine an acceptable level of under-sampling for the CS-RARE acquisitions, artificially under-sampled **k**-space data were generated by multiplying the fully-sampled 3D **k**-space data set by variable-density sampling patterns ranging from 12.5% to 75% sampling. A summary of the ℓ_2-error, PSNR and SSIM for the best CS reconstruction and zero-filled Fourier transform at the different levels of under-sampling that have been tested is shown in Fig. 8. As expected, it is seen that the CS reconstructions outperform the zero-filled Fourier transform. Furthermore, the enhancement in the quality of the CS reconstructions, relative to the zero-filled Fourier transforms increases with the level of under-sampling. Two-dimensional *xz* slice images from the central plane of the 3D images of the CS reconstructions are shown in Fig. 9a–e for 12.5, 25, 37.5, 50 and 75% sampling, respectively. From Fig. 9 it is seen that at all levels of under-sampling, the edges of the rock are clearly resolved however, the fine-detailed structures in the image appear to be progressively more smoothed as the extent to which **k**-space is under-sampled increases. It can also be seen that certain coarser-scale features in the image, such as the 'pocket' of air or non-porous solid circled in Fig. 9a), are preserved even at the highest degree of under-sampling that has been considered. In order to be able to resolve core-scale phenomena that are of interest in laboratory core floods, such as Saffman-Taylor instabilities [12,36] and capillary end effects [9], it is information on the millimetre to centimetre scale that is required. Therefore, the loss of contrast at the pore-scale level is deemed acceptable in the present application. Considering the results presented in Fig. 9, a **k**-space sampling fraction of 25% has been used for the subsequent 3D

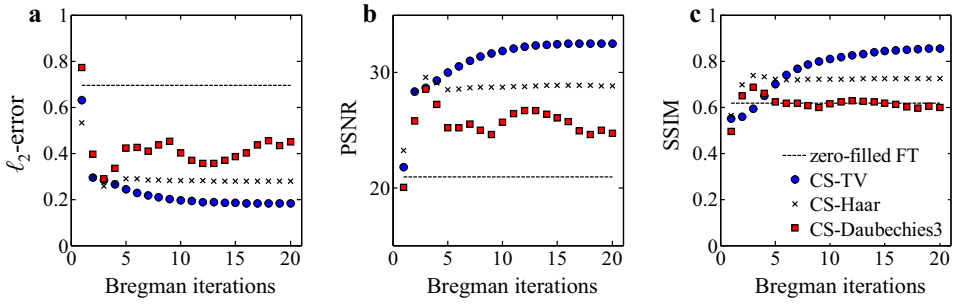

Fig. 6. (a) ℓ_2-error, (b) PSNR and (c) SSIM of the images obtained using a Total Variation, Haar wavelet and Daubechies3 wavelet as the regularisation functional in the CS reconstructions of the 25% sampled **k**-space. Each metric indicates that the CS reconstructions outperform the zero-filled Fourier transform and that of the regularisation functionals tested, Total Variation yields the highest quality reconstruction.

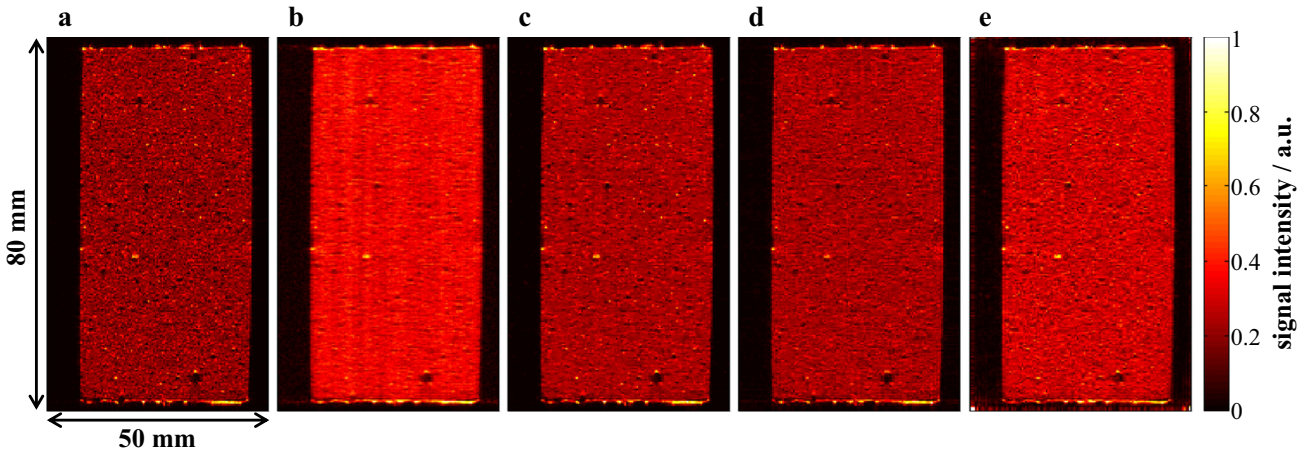

Fig. 7. 2D *xz* slice images from the central plane of the 3D images obtained from the (a) fully sampled 3D image, (b) zero-filled Fourier transform of the 25% sampled **k**-space data, and CS reconstructions of the 25% sampled **k**-space data sets using (c) TV, and (d) Haar and (e) Daubechies3 wavelet transforms as the regulariser. The intensity scale for each image has been normalised relative to the maximum intensity pixel in that image and is proportional to the local water content in the rock.

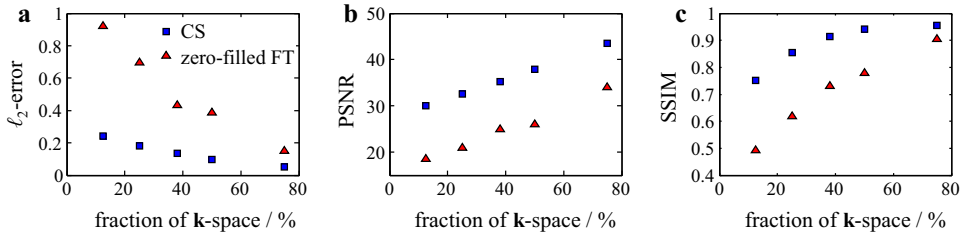

Fig. 8. (a) ℓ_2-error, (b) PSNR and (c) SSIM of the images obtained using a zero-filled Fourier transform and total variation as the regulariser in the CS reconstructions for **k**-space sampling fractions ranging from 12.5% to 75%.

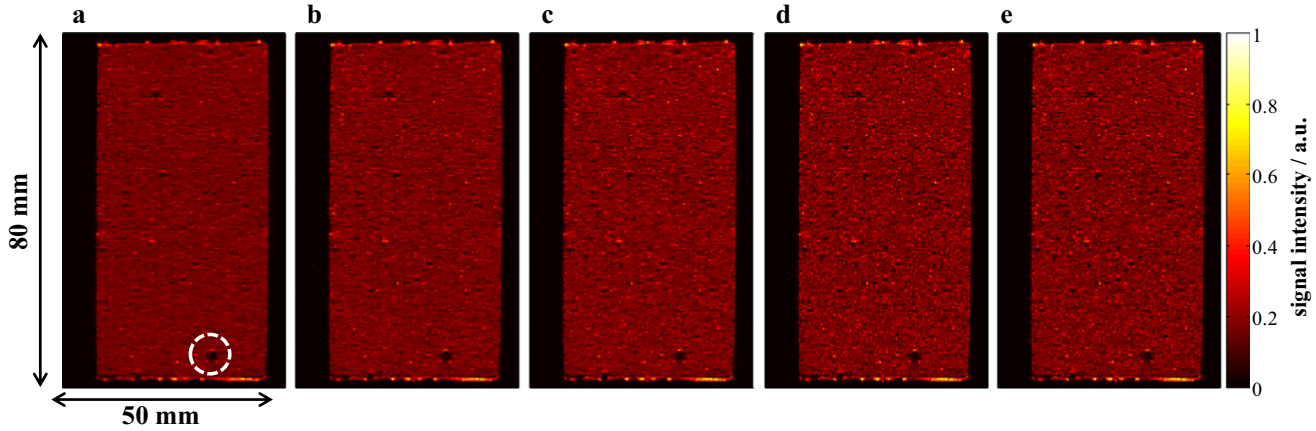

Fig. 9. 2D *xz* slice images from the central plane of the 3D images obtained from the CS reconstructions of the (a) 12.5%, (b) 25%, (c) 37.5%, (d) 50% and (e) 75% sampled **k**-space data using TV as the regulariser. The intensity scale for each image has been normalised relative to the maximum intensity pixel in that image and is proportional to the local water content in the rock. The highlighted region in (a) identifies a 'pocket' of air or non-porous solid within the rock.

CS-RARE acquisitions. With a 25% sampling of **k**-space, a RARE factor of $N_{RF} = 64$ and eight scans for signal averaging, the resulting acquisition time was ~16 min. This level of under-sampling has been chosen so as to achieve a balance between the enhancement in the temporal resolution of the image acquisitions that is required to investigate the dynamics of the core flood whilst maintaining fidelity in the CS reconstructions of both coarse and, to a certain degree, the finer-scale features in the image.

5.3. Water-water displacement and dodecane drainage

Fig. 10 shows the 3D CS-RARE images at various times during the core flood following injection of the doped-water solution. The signal intensity has been normalised relative to a reference image acquired prior to beginning the flow of the injectant. For subsequent images, a high-pass threshold has been applied such that voxels with intensity greater than 10% of the intensity of the

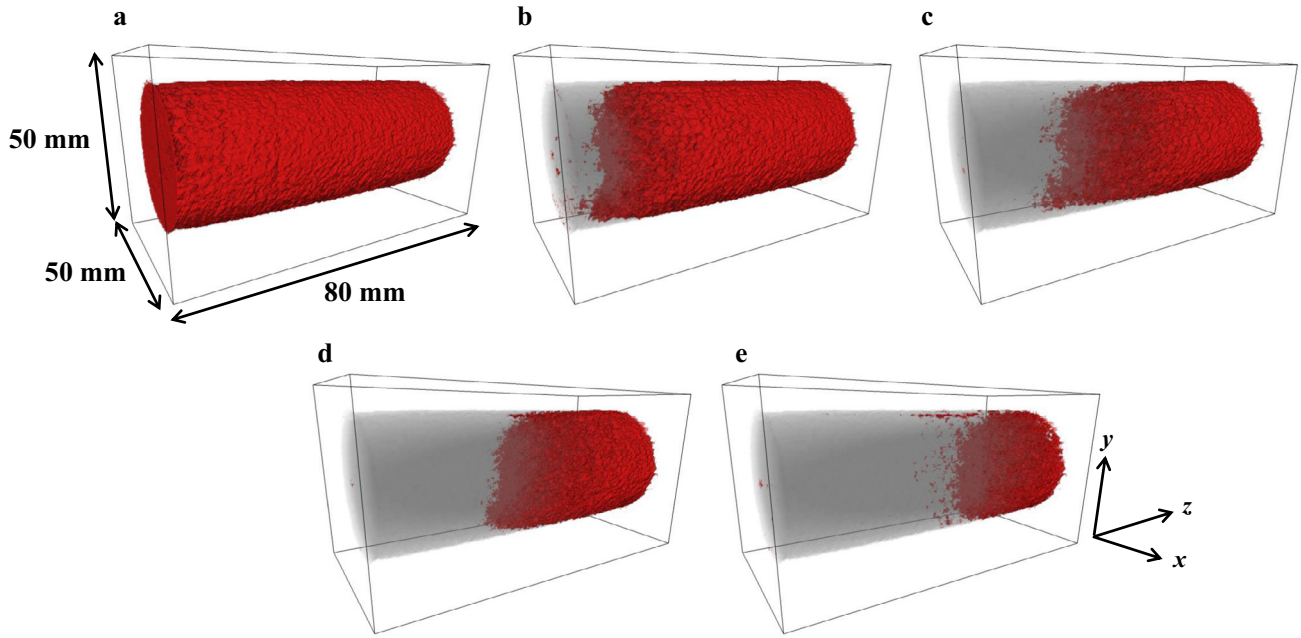

Fig. 10. 3D CS images of the residual water (red) in the Bentheimer rock core after (a) 0, (b) 64, (c) 128, (d) 192, (e) 256 min of flowing the $GdCl_3$ (aq) solution at 0.1 ml min^{-1}. The images of the residual water content indicate the distribution of the water that was initially in the rock. The flow of the injectant is from left-to-right, in the *z* direction. From the series of images, the invasion front throughout the core flood is evident. (For interpretation of the references to colour in this figure legend, the reader is referred to the web version of this article.)

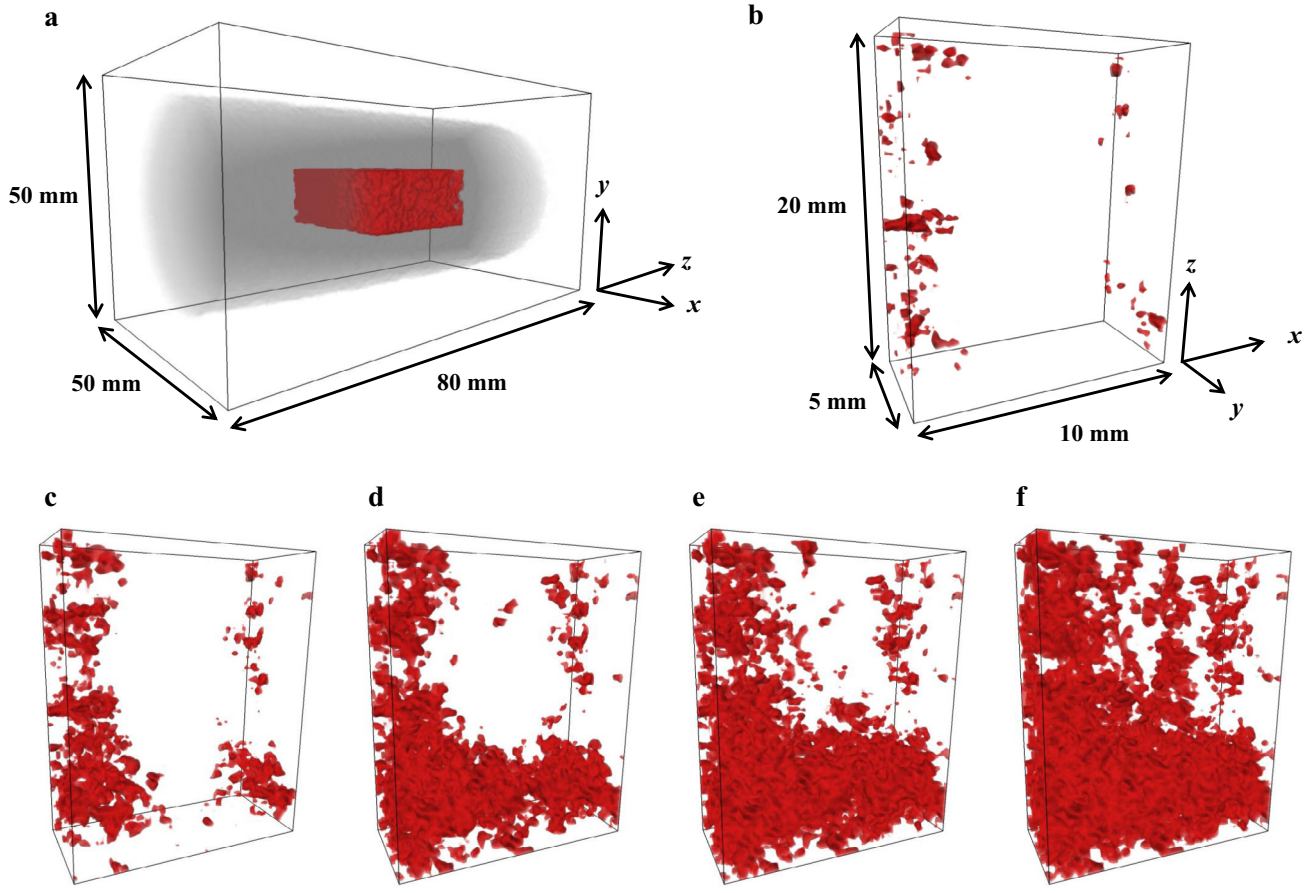

Fig. 11. (a) Location from which the 20 mm × 10 mm × 5 mm ($z \times x \times y$) region of interest is taken from within the rock and a series of 3D CS images at (b) 240 (c) 400, (d) 560, (e) 720, (f) 840 min during the primary drainage of dodecane into the water-saturated Bentheimer plug. Red indicates dodecane, whilst the water is not detected in the image. The flow of dodecane is in the *z* direction. (For interpretation of the references to colour in this figure legend, the reader is referred to the web version of this article.)

reference image are assigned to be residual water and appear as red in the image.

From Fig. 10, the progress of the displacement front through the rock during the core flood is clearly observed. With the flow rate of 0.1 ml min^{-1}, corresponding to an interstitial velocity of $v_i = 1.89 \pm 0.03$ ft day^{-1}, 0.1 P.V. of the injectant has been injected over the period of each 16 min acquisition. For fully-sampled spin-warp and RARE images acquired using the same acquisition parameters as the CS-RARE images presented in Fig. 10, the total injected pore volumes would be 12.3 P.V. and 0.4 P.V. respectively. From this analysis, it is evident that the 3D CS-RARE technique enables a more accurate measurement of the fluid saturation within the rock at specific time points in the core flood experiment.

Following the imbibition of the doped water solution, dodecane was injected into the water-saturated rock core at a flow rate of 0.1 ml min^{-1}. At this stage none of the residual water could be detected in the image and it is assumed that the entire signal is from the dodecane. A series of images during this dodecane drainage process from a 20 mm × 10 mm × 5 mm region of interest (ROI) in the rock core are presented in Fig. 11. The location of the ROI within the rock core is shown in Fig. 11a).

From Fig. 11, it is seen that the dodecane advances into the pore space in the form of discrete clusters before coalescing to form a continuous, connected pathway of the non-wetting phase at higher saturations. The observation that the dynamics of this process can be studied with both the spatial and temporal resolution presented herein, demonstrates the potential to investigate important processes involving the flow of multiple immiscible phases in porous media using MRI.

6. Conclusions

In this paper, a method using the RARE pulse sequence with CS for 3D imaging of the fluid saturation in rocks during a laboratory core flood has been demonstrated. To achieve this implementation, both the **k**-space sampling scheme and regularisation functional used in the CS reconstructions were optimised. With respect to the **k**-space sampling scheme, it has been shown that sampling k_{P1} and k_{P2} according to a two-dimensional as opposed to a series of one-dimensional pseudo-random variable density sampling schemes yields better results in terms of minimising the coherence of the under-sampling artefacts in the linear reconstruction. Further, a novel method for the acquisition of under-sampled 3D **k**-space data using the RARE pulse sequence has been presented whereby the coefficients of $k_{P1,2}$ are sampled in an order corresponding to their distance from the centre of **k**-space.

An objective method for determining the optimal regularisation functional to be used in the CS reconstructions has also been presented. All three metrics that have been considered indicate that, in the present application, TV yields the best image quality with respect to a fully-sampled 'ground truth' image. For a 25% **k**-space sampling fraction, an image with an ℓ_2-error = 0.18, PSNR = 32.5 and an SSIM = 0.86 is recovered.

For the present application, a **k**-space sampling fraction of 25% was chosen resulting in an acquisition time of 16 min. Relative to the fully-sampled image, with the same RARE factor, this was a four-fold reduction in the acquisition time however greater time savings are possible over more standard pulse sequences. Finally, the CS-RARE technique has been applied to image the residual water saturation during a water-water displacement laboratory core flood and subsequently the drainage of dodecane into the water-saturated rock. The enhancement in the temporal resolution has enabled the fluid distribution to be monitored on a time-scale that would not be possible using conventional 3D MRI protocols.

The reduction in acquisition times using CS will provide the ability to investigate dynamic systems, such as laboratory core floods, using 3D MRI with a much greater temporal resolution. The implementation of this approach in rock core analysis will also be beneficial as the time savings can be used to make other measurements, such as T_1–T_2 and D–T_2, to enable a more holistic characterisation of the displacement process or to improve the SNR of the acquisition through a greater number of signal averages per unit time.

Acknowledgments

The authors would like to thank Royal Dutch Shell plc for funding this work. LFG and AJS also wish to thank EPSRC for financial support (EP/K039318/1). MB also thanks EPSRC for financial support (EP/M00483X/1).

References

[1] E. Aspenes, G. Ersland, A. Graue, J. Stevens, B.A. Baldwin, Wetting phase bridges establish capillary continuity across open fractures and increase oil recovery in mixed-wet fractured chalk, Transport Porous Med. 74 (2007) 35–47.
[2] J. Mitchell, J. Staniland, R. Chassagne, E.J. Fordham, Quantitative in situ enhanced oil recovery monitoring using nuclear magnetic resonance, Transport Porous Med. 94 (2012) 683–706.
[3] S.M. Arora, D. Horstmann, P.K. Cherukupalli, J.E. Edwards, R. Ramamoorthy, T. D. McDonald, D.C. Bradley, C. Ayan, J. Zaggas, K. Cig, SPE 129069 Single-well in-situ measurement of residual oil saturation after an EOR chemical flood, in: SPE EOR Conference at Oil & Gas West Asia, Muscat, Oman, 11–13 April 2010, Society of Petroleum Engineers, Muscat, Oman, 2010, p. SPE paper 129069.
[4] J. Mitchell, J. Staniland, A. Wilson, A. Howe, A. Clarke, E.J. Fordham, J. Edwards, R. Faber, R. Bouwmeester, Magnetic resonance imaging of chemical EOR in core to complement field pilot studies, in: International Symposium of the Society of Core Analysts, Aberdeen Scotland, UK, 27–30 August 2012, Society of Core Analysts, Aberdeen, Scotland, 2012, p. SCA Paper 2012-30.
[5] Z. Yuechao, S. Yongchen, L. Yu, J. Lanlan, Z. Ningjun, Visualization of CO_2 and oil immiscible and miscible flow processes in porous media using NMR micro-imaging, Petrol. Sci. 8 (2011) 183–193.
[6] K.E. Washburn, G. Madelin, Imaging of multiphase fluid saturation within a porous material via sodium NMR, J. Magn. Resonance 202 (2010) 122–126.
[7] J.S. Archer, S.W. Wong, Use of a reservoir simulator to interpret laboratory waterflood data, in: SPE-AIME 46th Annual Full Meeting. New Orelans, 3–6 Oct 1973, Society of Petroleum Engineers, New Orleans, 1973, p. SPE paper 3551.
[8] M.P. Enwere, J.S. Archer, NMR imaging for water/oil displacement in cores under viscous-capillary force control, in: SPE Eighth Symposium on Enhanced Oil Recovery, Tulsa, Oklahoma, 22–24 April 1992, Society of Petroleum Engineers, Tulsa, Oklahoma, 1992, p. SPE Paper 24166.
[9] D.D. Huang, M.M. Honarpour, Capillary end effects in coreflood calculations, in: International Symposium of the Society of Core Analysts, Montpellier, France, 8–10 September 1996, Society of Core Analysts, Montpellier, France, 1996, p. SCA Paper 9634.
[10] G. Ersland, J. Husebø, A. Graue, B. Kvamme, Transport and storage of CO_2 in natural gas hydrate reservoirs, Energy Proc. 1 (2009) 3477–3484.
[11] G. Ersland, J. Husebø, A. Graue, B.A. Baldwin, J. Howard, J. Stevens, Measuring gas hydrate formation and exchange with CO_2 in Bentheim sandstone using MRI tomography, Chem. Eng. J. 158 (2010) 25–31.
[12] Y. Liu, Y. Song, Y. Zhao, T. Wang, L. Jiang, MRI study on CO_2 flooding characteristics in n-decane saturated glass bead packs, Proc. Environ. Sci. 11 (2011) 650–654.
[13] N. Loahardjo, N.R. Morrow, J. Stevens, J. Howard, Nuclear magnetic resonance imaging: application to determination of saturation changes in a sandstone core by sequential waterflooding, in: International Symposium of the Society of Core Analysts, Halifax, Nova Scotia, Canada, 4–7 October 2010, Society of Core Analysts, Halifax, Nova Scotia, Canada, 2010, p. SCA Paper 2010-16.
[14] J. Mitchell, J.E. Edwards, E. Fordham, J. Staniland, R. Chassagne, P.K. Cherukupalli, O.B. Wilson, M.J. Faber, R. Bouwmeester, Quantitative remaining oil interpretation using magnetic resonance: from the laboratory to the pilot, in: SPE EOR Conference at Oil & Gas West Asia, Muscat, Oman, 16–18 April 2012, Society of Petroleum Engineers, Muscat, Oman, 2012, p. SPE 154704.
[15] J. Mitchell, J. Staniland, R. Chassagne, K. Mogensen, S. Frank, E.J. Fordham, Mapping oil saturation distribution in a limestone plug with low-field magnetic resonance, J. Petrol. Sci. Eng. 108 (2013) 1–8.
[16] L.B. Romero-Zerón, L. Li, S. Ongsurakul, B.J. Balcom, Visualization of waterflooding through unconsolidated porous media using magnetic resonance imaging, Pet. Sci. Technol. 27 (2009) 1993–2009.
[17] L.B. Romero-Zerón, S. Ongsurakul, L. Li, B.J. Balcom, Visualization of the effect of porous media wettability on polymer flooding performance through unconsolidated porous media using magnetic resonance imaging, Pet. Sci. Technol. 28 (2010) 52–67.

[18] Y. Song, N. Zhu, Y. Zhao, Y. Liu, L. Jiang, T. Wang, Magnetic resonance imaging study on near miscible supercritical CO_2 flooding in porous media, Phys. Fluids 25 (2013) 053301.
[19] T. Suekane, N. Furukawa, S. Tsushima, S. Hirai, M. Kiyota, Application of MRI in the measurement of two-phase flow of supercritical CO_2 and water in porous rocks, J. Porous Media 12 (2009) 143–154.
[20] Y. Wang, T. Luce, C. Ishizawa, M. Shuck, K. Smith, H. Ott, M. Appel, Halite precipitation and permeability assessment during supercritical CO_2 core flood, in: International Symposium of the Society of Core Analysts, Halifax, Nova Scotia, Canada, 4–7 October 2010, Society of Core Analysts, Halifax, Nova Scotia, Canada, 2010, p. SCA Paper 2010-18.
[21] A. Brautaset, G. Ersland, A. Graue, J. Stevens, J. Howard, Using MRI to study in situ oil recovery during CO_2 injection in carbonates, in: International Symposium of the Society of Core Analysts, Abu Dhabi, UAE, 29 October–2 November 2008, Society of Core Analysts, Abu Dhabi, UAE, 2008: p. SCA paper 2008–41.
[22] G. Ersland, M.A. Fernø, A. Graue, B.A. Baldwin, J. Stevens, Complementary imaging of oil recovery mechanisms in fractured reservoirs, Chem. Eng. J. 158 (2010) 32–38.
[23] M.A. Fernø, G. Ersland, Å. Haugen, E. Johannesen, A. Graue, J. Stevens, J. Howard, Impacts from fractures on oil recovery mechanisms in carbonate rocks at oil-wet and water-wet conditions – visualizing fluid flow across fractures with MRI, in: 2007 International Oil Conference and Exhibition, Veracruz, Mexico, 27–30 June 2007, Society of Petroleum Engineers, Veracruz, Mexico, 2007, p. SPE paper 108699.
[24] A. Andrianov, R. Farajzadeh, M.M. Nick, M. Talanana, P.L.J. Zitha, Immiscible foam for enhancing oil recovery: bulk and porous media experiments, Ind. Eng. Chem. Res. 51 (2012) 2214–2226.
[25] Å. Haugen, N. Mani, S. Svenningsen, B. Brattekås, A. Graue, G. Ersland, et al., Miscible and immiscible foam injection for mobility control and EOR in fractured oil-wet carbonate rocks, Transport Porous Med. 104 (2014) 109–131.
[26] M. Kumar, T.J. Senden, A.P. Sheppard, J.P. Middleton, M.A. Knackstedt, Visualizing and quantifying the residual phase distribution in core material, in: International Symposium of the Society of Core Analysts, Noordwijk, The Netherlands, 27–30 September 2009, Society of Core Analysts, Noordwijk, The Netherlands, 2009, p. SCA Paper 2009-016.
[27] S. Youssef, E. Rosenberg, H. Deschamps, R. Oughanem, E. Maire, R. Mokso, Oil ganglia dynamics in natural porous media during surfactant flooding captured by ultra-fast x-ray microtomography, in: International Symposium of the Society of Core Analysts, Avignon, France, 11–18 September 2014, Society of Core Analysts, Avignon, France, 2014, p. SCA Paper 2014-023.
[28] T. Suekane, N.H. Thanh, T. Matsumoto, M. Matsuda, M. Kiyota, A. Ousaka, Direct measurement of trapped gas bubbles by capillarity on the pore scale, Energy Proc. 1 (2009) 3189–3196.
[29] A.L. Herring, E.J. Harper, L. Andersson, A. Sheppard, B.K. Bay, D. Wildenschild, Effect of fluid topology on residual nonwetting phase trapping: Implications for geological CO_2 sequestration, Adv. Water Resour. 62 (2013) 47–58.
[30] H.J. Vinegar, X-ray CT and NMR imaging of rocks, J. Petrol. Technol. 38 (1986) 257–259.
[31] S. Davies, K.J. Packer, Pore-size distributions from nuclear magnetic resonance spin-lattice relaxation measurements of fluid-saturated porous solids. I. Theory and simulation, J. Appl. Phys. 67 (1990) 3163–3170.
[32] S. Davies, K.J. Packer, D.R. Roberts, F.O. Zelaya, Pore-size distributions from NMR spin-lattice relaxation data, Magn. Reson. Imag. 9 (1991) 681–685.
[33] D.P. Gallegos, K. Munn, D.M. Smith, D.L. Stermer, A NMR technique for the analysis of pore structure: application to materials with well-defined pore structure, J. Colloid Interf. Sci. 119 (1987) 127–140.
[34] J. Mitchell, M.D. Hürlimann, E.J. Fordham, A rapid measurement of T_1/T_2: the DECPMG sequence, J. Magn. Reson. 200 (2009) 198–206.
[35] J. Mitchell, T.C. Chandrasekera, D.J. Holland, L.F. Gladden, E.J. Fordham, Magnetic resonance imaging in laboratory petrophysical core analysis, Phys. Rep. 526 (2013) 165–225.
[36] P.G. Saffman, G. Taylor, The penetration of a fluid into a porous medium or Hele-Shaw cell containing a more viscous liquid, Proc. Roy. Soc. London A 245 (1958) 312–329.
[37] H. Ott, S. Oedai, Wormhole formation and compact dissolution in single- and two-phase CO_2-brine injections, Geophys. Res. Lett. 42 (2015) 2270–2276.
[38] H. Nyquist, Certain topics in telegraph transmission theory, Trans. AIEE 47 (1928) 617–644.
[39] C.E. Shannon, Communication in the presence of noise, Proc. IRE 37 (1949) 10–21.
[40] W.A. Edelstein, J.M.S. Hutchison, G. Johnson, T. Redpath, Spin warp NMR imaging and applications to human whole-body imaging, Phys. Med. Biol. 25 (1980) 751–756.
[41] J. Hennig, A. Nauerth, H. Friedburg, RARE imaging: a fast imaging method for clinical MR, Magn. Reson. Med. 3 (1986) 823–833.
[42] P. Mansfield, Multi-planar image formation using NMR spin echoes, J. Phys. C 10 (1977) L55–L58.
[43] M. Lustig, D. Donoho, J.M. Pauly, Sparse MRI: The application of compressed sensing for rapid MR imaging, Magn. Reson. Med. 58 (2007) 1182–1195.
[44] M. Lustig, D.L. Donoho, J.M. Santos, J.M. Pauly, Compressed sensing MRI, IEEE Signal Process Mag 25 (2008) 72–82.
[45] P. Parasoglou, D. Malioutov, A.J. Sederman, J. Rasburn, H. Powell, L.F. Gladden, et al., Quantitative single point imaging with compressed sensing, J. Magn. Reson. 201 (2009) 72–80.
[46] O.V. Petrov, B.J. Balcom, Two-dimensional T_2 distribution mapping in porous solids with phase encode MRI, J. Magn. Reson. 212 (2011) 102–108.
[47] D. Xiao, B.J. Balcom, Two-dimensional T_2 distribution mapping in rock core plugs with optimal **k**-space sampling, J. Magn. Reson. 220 (2012) 70–78.
[48] D. Xiao, B.J. Balcom, Restricted **k**-space sampling in pure phase encode MRI of rock core plugs, J. Magn. Reson. 231 (2013) 126–132.
[49] D. Xiao, B.J. Balcom, K-*t* acceleration in pure phase encode MRI to monitor dynamic flooding processes in rock core plugs, J. Magn. Reson. 243 (2014) 114–121.
[50] D.N. Guilfoyle, B. Issa, P. Mansfield, Rapid volumetric NMR imaging of fluids in porous solids using a 3D π-EPI (PEPI) hybrid, J. Magn. Reson. A 119 (1996) 151–156.
[51] D. Xiao, B.J. Balcom, Π echo-planar imaging with concomitant field compensation for porous media MRI, J. Magn. Reson. 260 (2015) 38–45.
[52] M. Li, D. Xiao, L. Romero-Zerón, F. Marica, B. MacMillan, B.J. Balcom, Mapping three-dimensional oil distribution with π-EPI MRI measurements at low magnetic field, J. Magn. Reson. 269 (2016) 13–23.
[53] M. Benning, L.F. Gladden, D.J. Holland, C.-B. Schonlieb, T. Valkonen, Phase reconstruction from velocity-encoded MRI measurements – a survey of sparsity-promoting variational approaches, J. Magn. Reson. 238 (2014) 26–43.
[54] D.J. Holland, L.F. Gladden, Less is More: how compressed sensing is transforming metrology in chemistry, Angew. Chem. Int. Ed. 53 (2014) 13330–13340.
[55] Z. Wang, A.C. Bovik, H.R. Sheikh, E.P. Simoncelli, Image quality assessment: from error visibility to structural similarity, IEEE T Image Process. 13 (2004) 600–612.